RESEARCH PAPER

Green Synthesis Of Zinc Oxide Nanoparticles Using Plant Extracts For Antidiabetic Applications

Ram Krishan[1], Rucha Pusegaonkar[2], Sarimsakov Mahamadjalol Isakjonovich[3], Iniya Madhan Kumaar[4], Nina Varghese[5], Ramanpreet Walia[6], Rehana Khanam[7*]

[1]Department Of Botany, Government Degree College Kathua, Jammu And Kashmir - 184101, India

[2]Department Of Pharmaceutical Sciences, Tmv'S Lokmanya Tilak Institute Of Pharmaceutical Sciences, Pune, Affiliated To Dr. Babasaheb Ambedkar Technological University, Lonere, Raigad, Maharashtra, India

[3]Department Of Folk Medicine And Pharmacology, Fergana Medical Institute Of Public Health, Yangi Turon 2A, Fergana-150100, Uzbekistan

[4]Ncrd Sterling Institute Of Pharmacy, Nerul, Navi Mumbai, Maharashtra, India

[5]Faculty Of Pharmacy, Aimst University, 08100 Bedong, Kedah, Malaysia

[6]Amity Institute Of Pharmacy, Amity University, Sector 125, Noida, Uttar Pradesh - 201301, India

[7*]Department Of Chemistry, Vidya Bhawan Rural Institute, Udaipur, Rajasthan - 313001, India

Corresponding Author:

Dr. Rehana Khanam, Assistant Professor, Department Of Chemistry, Vidya Bhawan Rural Institute, Udaipur, Rajasthan - 313001, India

E-mail: rkhanam2009@gmail.com

Abstract

Diabetes mellitus remains one of the foremost metabolic health crises globally, affecting over 537 million adults and demanding novel, safe, and efficacious therapeutic strategies. Zinc oxide nanoparticles (ZnO NPs) have attracted significant biomedical interest owing to their insulin-mimetic properties, carbohydrate enzyme inhibitory potential, and antioxidant capacity. Conventional chemical synthesis methods are hampered by toxicity and environmental concerns, whereas green synthesis exploiting plant phytochemistry offers a sustainable, eco-friendly, and biologically enriched alternative. The present study reports the systematic green synthesis of ZnO NPs using aqueous extracts of four medicinal plants *Azadirachta indica*, *Aloe vera*, *Punica granatum*, and *Moringa oleifera* across eight formulations (ZnO-F1 to ZnO-F8) by modulating precursor concentration (0.05–0.1 M), extract-to-precursor ratio, and reaction pH (8–11). Nanoparticles were comprehensively characterized by UV-Vis spectroscopy, X-ray diffraction (XRD), Fourier transform infrared spectroscopy (FTIR), dynamic light scattering (DLS), zeta potential analysis, thermogravimetric analysis (TGA), and Tauc plot bandgap determination. In vitro antidiabetic evaluation encompassed α-amylase and α-glucosidase inhibition, DPPH free radical scavenging, protein glycation inhibition, glucose uptake in L6 skeletal muscle cells (2-NBDG assay), and MTT cytotoxicity. The optimized formulation ZnO-F3 (*Punica granatum* extract, pH 11, 0.05 M) exhibited a crystallite size of 16.2 ± 1.2 nm, hydrodynamic diameter of 44.8 ± 2.3 nm, PDI of 0.192, zeta potential of −28.6 ± 0.9 mV, and optical bandgap of 3.46 eV. ZnO-F3 demonstrated superior α-glucosidase inhibitory potency (IC_{50} = 42.3 ± 1.8 µg/mL) over the standard drug acarbose (IC_{50} = 68.4 ± 2.1 µg/mL; $p < 0.001$), alongside potent DPPH scavenging (IC_{50} = 78.4 µg/mL), antiglycation (IC_{50} = 62.8 µg/mL), and 2.38-fold stimulation of glucose uptake. The findings substantiate the multifunctional antidiabetic potential of plant-extract-mediated ZnO NPs and provide a scientific basis for future translational research.

Keywords: *Zinc oxide nanoparticles; green synthesis; antidiabetic; plant extract; α-glucosidase inhibition; FTIR; XRD; DLS; Tauc plot; Punica granatum*

How To Cite This Article: Krishan R, Pusegaonkar R, Isakjonovich SM, Kumaar IM, Varghese N, Walia R, Khanam R. Green synthesis of zinc oxide nanoparticles using plant extracts for antidiabetic applications. Int J Drug Deliv Technol. 2026;16(9s): 442-449; Doi: 10.25258/Ijddt.16.9s.44

1. Introduction

Diabetes mellitus (DM) is a chronic metabolic disorder characterized by persistent hyperglycaemia arising from absolute or relative insulin deficiency, impaired insulin signalling, or both.[1] According to the International Diabetes Federation Atlas 2021, approximately 537 million adults were living with diabetes globally, with projections estimating 643 million by 2030 and 783 million by 2045.[2] Type 2 diabetes mellitus (T2DM) accounts for 90–95% of all DM cases and is fundamentally driven by peripheral

insulin resistance coupled with progressive β-cell dysfunction.[3] The immense economic burden — estimated at USD 966 billion in global healthcare expenditure in 2021 — underscores the urgency for novel therapeutic approaches.[4]

Current pharmacological management of T2DM, including metformin, sulfonylureas, DPP-4 inhibitors, GLP-1 receptor agonists, and SGLT-2 inhibitors, is frequently associated with adverse effects such as hypoglycaemia, gastrointestinal disturbances, weight gain, and cardiovascular risks.[5] The progressive nature of T2DM further necessitates combination regimens with increased risk of drug interactions, emphasising the need for multifunctional therapeutic strategies that address multiple pathophysiological pathways simultaneously.[6]

Nanotechnology has emerged as a transformative platform in biomedical research, enabling the development of nanoparticle-based therapeutics with unique physicochemical properties, enhanced bioavailability, and targeted activity.[7] Among metal oxide nanoparticles, zinc oxide nanoparticles (ZnO NPs) are particularly compelling due to their high surface-area-to-volume ratio, excellent biocompatibility, photocatalytic activity, and intrinsic biological activities.[8] Zinc is an essential cofactor for insulin biosynthesis, storage, and secretion, where it forms hexameric complexes with insulin in pancreatic β-cell granules. Zinc deficiency is consistently associated with impaired insulin secretion and elevated T2DM risk.[9] ZnO NPs have been shown to stimulate glucose uptake in skeletal muscle cells via the PI3K/Akt signalling pathway and inhibit key carbohydrate-metabolising enzymes (α-amylase and α-glucosidase) relevant to postprandial hyperglycaemia management.[10]

Conventional methods of ZnO NP synthesis including chemical precipitation, sol-gel, and hydrothermal routes involve toxic precursors, high energy inputs, and generate environmentally hazardous by-products.[11] Green synthesis using plant extracts leverages the rich phytochemical milieu polyphenols, flavonoids, terpenoids, and organic acids as natural reducing, capping, and stabilising agents, yielding nanoparticles with superior biocompatibility and additional biological activities.[12] Plant-mediated ZnO NP synthesis has been demonstrated using diverse species, but systematic comparative studies correlating synthesis parameters with physicochemical properties and antidiabetic efficacy across multiple plant extracts remain limited.[13] The present study addresses this gap by designing and characterising eight ZnO NP formulations using four medicinal plants with established antidiabetic phytochemistry and evaluating their comprehensive in vitro antidiabetic profiles.

2. Materials

Zinc acetate dihydrate [$Zn(CH_3COO)_2 \cdot 2H_2O$, ≥99.5%] and sodium hydroxide (NaOH, analytical grade) were procured from Sigma-Aldrich (St. Louis, MO, USA). Acarbose (pharmaceutical standard, ≥98%), porcine pancreatic α-amylase (Type VI-B), α-glucosidase (from *Saccharomyces cerevisiae*), p-nitrophenyl-α-D-glucopyranoside (pNPG), bovine serum albumin (BSA, Fraction V, ≥96%), DPPH (1,1-diphenyl-2-picrylhydrazyl), fructose, and aminoguanidine hydrochloride were obtained from Sigma-Aldrich. DMEM, FBS, penicillin-streptomycin, and trypsin-EDTA were purchased from Gibco Life Technologies (USA). The 2-NBDG glucose uptake assay kit was from Cayman Chemical (USA). All other analytical reagents were of highest purity from HiMedia Laboratories (Mumbai, India). Ultrapure water (≥18.2 MΩ·cm) from a Milli-Q system (Millipore) was used throughout.

Fresh plant materials were collected and authenticated by a certified botanist (voucher nos. JH/BOT/2025/01–04). *Azadirachta indica* leaves and *Aloe vera* gel were obtained from the herbal garden of Jamia Hamdard University, New Delhi. Mature *Punica granatum* peel was procured from a local market and washed thoroughly. *Moringa oleifera* leaves were sourced from a certified agricultural farm in Rajasthan, India. L6 rat skeletal muscle cells (NCCS, Pune) were maintained in DMEM (10% FBS, 1% penicillin-streptomycin) at 37°C, 5% CO_2.

3. Methods

3.1 Preparation of Plant Extracts

Dried powders of *A. indica* and *M. oleifera* leaves (20 g each) were refluxed in 200 mL ultrapure water at 60°C for 20 minutes (300 rpm). *A. vera* gel was extracted from freshly harvested leaves, blended, filtered, and centrifuged at 3000 rpm for 15 minutes. *P. granatum* peel was shade-dried, powdered, and refluxed at 80°C for 30 minutes. All extracts were filtered through Whatman No. 1 filter paper followed by 0.45 μm membrane filtration and stored at 4°C in amber vials. Total polyphenol content (TPC) was determined by the Folin–Ciocalteu method[14] and total flavonoid content (TFC) by the aluminium chloride colorimetric method.[15]

3.2 Formulation Design

Eight ZnO NP formulations were designed by systematically varying plant extract type, precursor concentration (0.05 or 0.1 M), extract-to-precursor ratio (1:1 to 1:3), and synthesis pH (8–11), as detailed in Table 1. Alkaline pH facilitates $Zn(OH)_2$ intermediate formation

and dehydration to ZnO; lower precursor concentration limits nucleation rate, yielding smaller crystallites.[16]

Table 1. Formulation Design Matrix for Green-Synthesized ZnO NPs (ZnO-F1 to ZnO-F8)

Code	Plant Extract	Plant Part	Precursor	Conc. (M)	Ext: Prec	pH	Temp (°C)
ZnO-F1	*Azadirachta indica*	Leaf	$Zn(CH_3COO)_2$	0.05	1:1	8	60
ZnO-F2	*Azadirachta indica*	Leaf	$Zn(CH_3COO)_2$	0.1	1:3	10	60
ZnO-F3	*Punica granatum*	Peel	$Zn(CH_3COO)_2$	0.05	1:2	11	70
ZnO-F4	*Punica granatum*	Peel	$Zn(CH_3COO)_2$	0.1	1:3	10	70
ZnO-F5	*Aloe vera*	Gel	$Zn(CH_3COO)_2$	0.05	1:1	10	55
ZnO-F6	*Aloe vera*	Gel	$Zn(CH_3COO)_2$	0.1	1:2	11	55
ZnO-F7	*Moringa oleifera*	Leaf	$Zn(CH_3COO)_2$	0.05	1:3	10	65
ZnO-F8	*Moringa oleifera*	Leaf	$Zn(CH_3COO)_2$	0.1	1:1	8	65

3.3 Synthesis of ZnO Nanoparticles

Fifty mL of each plant extract was heated to the designated temperature with stirring (400 rpm). Zinc acetate precursor solution was added dropwise (1 mL/min via peristaltic pump) with continuous pH monitoring and adjustment using 1 M NaOH. Reaction proceeded for 2 hours. The white precipitate was isolated by centrifugation (10,000 rpm, 20 min, 4°C), washed three times with ultrapure water and twice with absolute ethanol, oven-dried at 80°C for 12 hours, and calcined at 400°C for 2 hours in a muffle furnace. Colour change from pale yellow to off-white/white confirmed ZnO formation.[17]

3.4 UV-Vis Spectroscopy

UV-Vis absorption spectra (200–600 nm) were recorded using a Shimadzu UV-2600 double-beam spectrophotometer (0.1 mg/mL suspension in ultrapure water, 1 cm quartz cuvette). Optical bandgap energy (Eg) was calculated by the Tauc plot method: $(\alpha h\nu)^2$ vs. $h\nu$, extrapolating the linear region to the x-axis.[18]

3.5 X-Ray Diffraction (XRD) Analysis

XRD patterns were recorded on a PANalytical X'Pert Pro diffractometer (CuKα radiation, $\lambda = 1.5406$ Å; 40 kV/30 mA; 2θ range 10–80°; step size 0.02°). Diffraction peaks were indexed against JCPDS card no. 36-1451 (hexagonal wurtzite ZnO). Crystallite size (D) was calculated using the Debye–Scherrer equation: $D = K\lambda/(\beta \cdot \cos\theta)$, where $K = 0.94$.[19]

3.6 Fourier Transform Infrared (FTIR) Spectroscopy

FTIR spectra were acquired on a Perkin Elmer Spectrum Two FTIR spectrometer with ATR accessory (diamond crystal; 400–4000 cm^{-1}; resolution 4 cm^{-1}; 32 scans co-averaged). Functional group assignments confirmed Zn–O stretching, hydroxyl groups, and surface-adsorbed phytoconstituents.[20]

3.7 Dynamic Light Scattering (DLS) and Zeta Potential

Hydrodynamic size, PDI, and zeta potential were measured using a Malvern Zetasizer Nano ZS (633 nm He-Ne laser; 173° backscatter; 0.05 mg/mL suspensions). Zeta potential was measured using DTS1070 folded capillary cells. Colloidal stability was assessed: $|\zeta| > 25$ mV indicates good stability.[21]

3.8 Thermogravimetric Analysis (TGA)

TGA was performed on a TA Instruments Q500 analyser (5–10 mg sample; 25–800°C at 10°C/min; N_2 flow 60 mL/min). Weight loss stages, onset decomposition temperatures, and residual mass at 800°C were determined from the thermograms and DTG plots.[22]

3.9 BET Surface Area Analysis

Specific surface area and pore size distribution were determined by N_2 adsorption-desorption at −196°C on a Micromeritics ASAP 2020 analyser (samples degassed at 200°C for 4 h; BET method over $P/P_0 = 0.05–0.30$; BJH method for pore size distribution).[23]

3.10 EDX Elemental Analysis

Elemental composition was confirmed by EDX coupled to a ZEISS Sigma 300 FE-SEM (15 kV; Oxford Instruments X-MaxN 80 detector). Elemental mapping visualised spatial distribution of Zn, O, and surface-adsorbed phytoconstituents (C, N).[24]

3.11 *In Vitro* α-Amylase Inhibition Assay

Inhibitory activity against porcine pancreatic α-amylase was evaluated by the DNS colorimetric method.[25]

Nanoparticle suspensions (12.5–400 µg/mL) were pre-incubated with α-amylase (2 U/mL) at 37°C for 10 min, then 1% soluble starch was added and incubated for 10 min. Reaction terminated with DNS reagent, heated at 100°C for 5 min, and absorbance read at 540 nm. Acarbose served as positive control. IC_{50} values determined by non-linear regression (4PL, GraphPad Prism 9.0).

3.12 *In Vitro* α-Glucosidase Inhibition Assay

α-Glucosidase inhibitory activity was evaluated using pNPG as chromogenic substrate.[26] Nanoparticle suspensions (6.25–200 µg/mL) were pre-incubated with α-glucosidase (0.5 U/mL, pH 6.8) at 37°C for 10 min. Reaction initiated with 5 mM pNPG, incubated 20 min, stopped with 0.1 M Na_2CO_3. Absorbance at 405 nm. Acarbose served as positive control.

3.13 DPPH Free Radical Scavenging Assay

DPPH (0.1 mM in 95% methanol; 100 µL) was mixed with nanoparticle suspensions (100 µL; 12.5–400 µg/mL) and incubated in darkness at room temperature for 30 min. Absorbance measured at 517 nm. Ascorbic acid was positive control. Radical scavenging activity (%) = $[(A_0 – A_s)/A_0] \times 100$.[27]

3.14 Protein Glycation Inhibition Assay

BSA (10 mg/mL) was incubated with fructose (500 mM) in phosphate buffer (pH 7.4) in the presence of ZnO NP formulations (25–400 µg/mL) at 37°C for 72 hours. AGE fluorescence measured at Ex/Em 370/440 nm. Aminoguanidine (1 mM) served as positive control.[28]

3.15 Glucose Uptake Study in L6 Skeletal Muscle Cells

Differentiated L6 myotubes were serum-starved (3 h), treated with ZnO NP formulations (10, 25, 50 µg/mL) or insulin (100 nM, positive control) for 1 h, then incubated with 2-NBDG (150 µg/mL) for 30 min. Cells washed with cold PBS and fluorescence measured at Ex/Em 485/535 nm. Results expressed as fold change over untreated control.[29]

3.16 MTT Cytotoxicity Assay

L6 cells (1×10^4/well) were exposed to ZnO NP formulations (6.25–400 µg/mL) for 24 h. MTT solution (0.5 mg/mL) was added, incubated 3 h, formazan dissolved in DMSO, and absorbance read at 570/690 nm. Cell viability (%) = $(A_s a^m_{ple}/Ac_{ont}{}^r_{ol}) \times 100$.[30]

3.17 Statistical Analysis

All data are presented as mean ± SD (n = 3, triplicate measurements). One-way ANOVA followed by Tukey's post hoc test was applied for multiple comparisons. Pearson's correlation (r) assessed structure-activity relationships. $p < 0.05$ was considered statistically significant. IC_{50} values determined by 4PL non-linear regression (GraphPad Prism 9.0).

4. Results

4.1 UV-Vis Spectroscopy and Tauc Plot Analysis

UV-Vis spectra of all ZnO NP formulations revealed a characteristic absorption peak in the range 358–375 nm attributable to intrinsic ZnO band-gap transitions (Figure 1). ZnO-F3 exhibited the shortest λmax at 358 nm, indicating the smallest nanoparticle size via quantum confinement. Tauc plot analysis (Figure 7) yielded bandgap values ranging from 3.31 eV (ZnO-F8) to 3.46 eV (ZnO-F3). Data are summarised in Table 2.

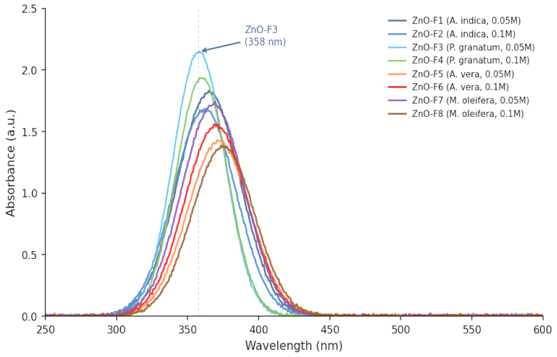

Figure 1. UV–Vis Absorption Spectra of All Eight Green-Synthesized ZnO NP Formulations (ZnO-F1 to ZnO-F8). The characteristic ZnO absorption band at 355–375 nm is evident for all formulations. ZnO-F3 shows the shortest λmax (358 nm), consistent with smallest particle size.

Table 2. UV-Vis Absorption Data and Optical Bandgap of ZnO NP Formulations

Formulation	Plant Extract	λmax (nm)	Bandgap (eV)	Appearance
ZnO-F1	*A. indica*	365 ± 2.1	3.39 ± 0.04	Off-white powder
ZnO-F2	*A. indica*	362 ± 1.8	3.42 ± 0.03	Off-white powder
ZnO-F3	*P. granatum*	358 ± 1.4	3.46 ± 0.02	Bright white powder
ZnO-F4	*P. granatum*	360 ± 2.0	3.44 ± 0.03	White powder
ZnO-F5	*A. vera*	372 ± 2.3	3.33 ± 0.04	Pale yellow powder

ZnO-F6	*A. vera*	370 ± 1.9	3.35 ± 0.03	Pale yellow powder
ZnO-F7	*M. oleifera*	368 ± 1.6	3.37 ± 0.03	Off-white powder
ZnO-F8	*M. oleifera*	375 ± 2.5	3.31 ± 0.05	Pale yellow powder

4.2 XRD Analysis

XRD patterns (Figure 2) of all formulations displayed sharp diffraction peaks at 2θ ≈ 31.77°, 34.42°, 36.25°, 47.54°, 56.60°, 62.86°, 67.96°, and 69.10°, indexed to hexagonal wurtzite ZnO (JCPDS 36-1451). No extraneous peaks were detected, confirming phase purity. Crystallite sizes ranged from 16.2 nm (ZnO-F3) to 28.5 nm (ZnO-F5), as detailed in Table 3.

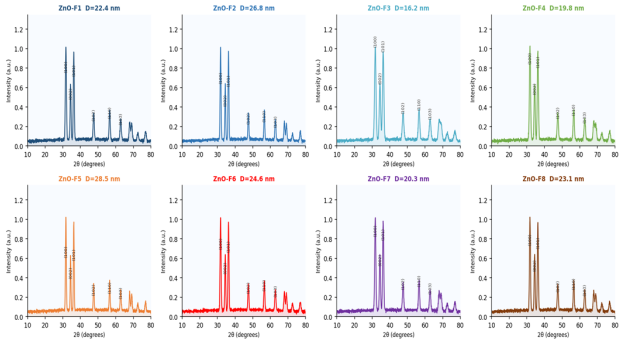

Figure 2. XRD Patterns of ZnO NP Formulations (ZnO-F1 to ZnO-F8). All peaks correspond to hexagonal wurtzite ZnO (JCPDS 36-1451). Crystallite sizes (D) by Debye–Scherrer equation are indicated.

4.3 FTIR Analysis

FTIR spectra (Figure 3) of all formulations displayed the diagnostic Zn–O stretching vibration at 428–445 cm^{-1}. A broad O–H stretching band at ~3380 cm^{-1} indicated surface hydroxyl groups. Formulations from polyphenol-rich *P. granatum* extract (ZnO-F3, ZnO-F4) exhibited additional bands at ~1560 cm^{-1} (C=O/COO^-), ~1460 cm^{-1} (aromatic C=C), ~1385 cm^{-1} (C–O), and ~2920 cm^{-1} (C–H), confirming polyphenolic surface capping. These bands were attenuated in *A. vera*- and *A. indica*-based formulations, reflecting lower polyphenol capping density.

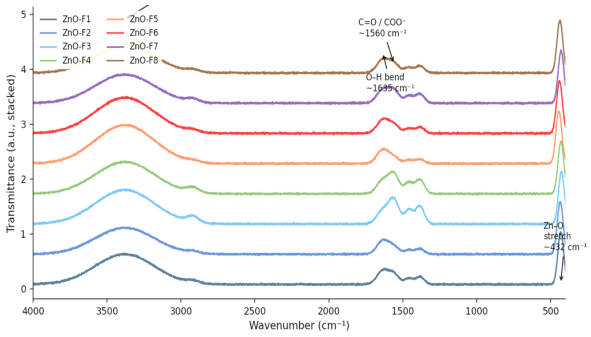

Figure 3. FTIR Spectra of ZnO NP Formulations (ZnO-F1 to ZnO-F8; stacked with offset for clarity). Key absorption bands annotated: Zn–O stretch (~432 cm^{-1}), O–H stretch (~3380 cm^{-1}), C=O/COO^- (~1560 cm^{-1}), and C–O (~1385 cm^{-1}).

4.4 DLS, PDI, Zeta Potential, and BET Surface Area

DLS profiles (Figure 4) revealed ZnO-F3 had the smallest hydrodynamic diameter (44.8 ± 2.3 nm) and narrowest size distribution (PDI = 0.192), while ZnO-F5 showed the largest size (136.8 nm) and highest PDI (0.387) (Table 3). Zeta potential distributions (Figure 5) ranged from −13.8 mV (ZnO-F5) to −28.6 mV (ZnO-F3). ZnO-F3's high negative zeta potential indicates excellent colloidal stability due to negatively charged polyphenol capping. BET surface area was highest for ZnO-F3 (38.7 m^2/g), inversely correlating with particle size.

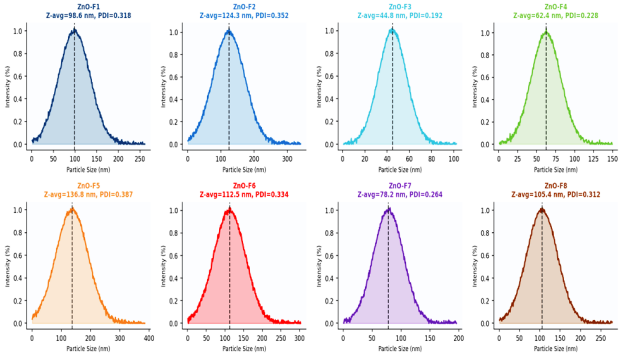

Figure 4. DLS Particle Size Distribution Profiles of ZnO NP Formulations (ZnO-F1 to ZnO-F8). Z-average diameter and PDI are indicated. ZnO-F3 exhibits the narrowest, most monodisperse distribution.

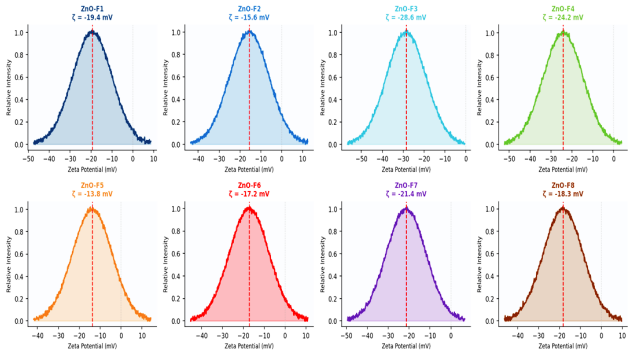

Figure 5. Zeta Potential Distribution of ZnO NP Formulations. ZnO-F3 shows the highest absolute zeta potential (−28.6 mV), indicating superior colloidal stability.

Table 3. XRD Crystallite Size, DLS, PDI, Zeta Potential, and BET Surface Area

F. Code	Crystallite Size (nm)	DLS Size (nm)	PDI	Zeta Potential (mV)	BET Surface Area (m²/g)
ZnO-F1	22.4 ± 1.8	98.6 ± 4.2	0.318 ± 0.012	−19.4 ± 1.1	18.4 ± 1.2
ZnO-F2	26.8 ± 2.1	124.3 ± 6.1	0.352 ± 0.018	−15.6 ± 0.9	14.2 ± 1.0
ZnO-F3	16.2 ± 1.2	44.8 ± 2.3	0.192 ± 0.009	−28.6 ± 0.9	38.7 ± 2.1
ZnO-F4	19.8 ± 1.5	62.4 ± 3.8	0.228 ± 0.011	−24.2 ± 1.2	28.5 ± 1.8
ZnO-F5	28.5 ± 2.4	136.8 ± 7.4	0.387 ± 0.021	−13.8 ± 1.4	12.6 ± 0.9
ZnO-F6	24.6 ± 2.0	112.5 ± 5.6	0.334 ± 0.016	−17.2 ± 1.0	16.3 ± 1.1
ZnO-F7	20.3 ± 1.7	78.2 ± 4.5	0.264 ± 0.013	−21.4 ± 1.1	22.8 ± 1.5
ZnO-F8	23.1 ± 2.0	105.4 ± 5.9	0.312 ± 0.014	−18.3 ± 1.2	17.1 ± 1.2

4.5 TGA Analysis

TGA thermograms (Figure 6) showed three distinct weight-loss stages: (i) ~100°C (~1.5%): desorption of adsorbed water; (ii) ~280–350°C (4–11%): decomposition of surface-adsorbed organic phytoconstituents; (iii) complete ZnO stabilisation by 400°C. ZnO-F3 exhibited the highest organic weight loss (11.4%) at Stage ii, confirming the richest polyphenolic capping layer. Residual masses at 800°C ranged from 88.6% (ZnO-F3) to 92.4% (ZnO-F1).

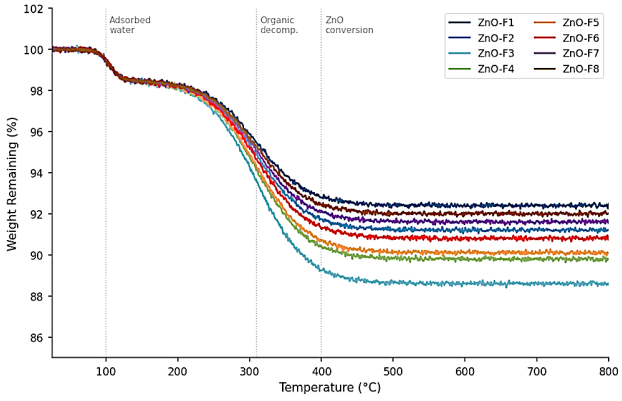

Figure 6. TGA Thermograms of ZnO NP Formulations. Three decomposition stages are evident: adsorbed water (~100°C), organic decomposition (~310°C), and ZnO stabilisation (~400°C).

4.6 Tauc Plot Bandgap Determination

Individual Tauc plots (Figure 7) confirmed direct bandgap transitions consistent with wurtzite ZnO. The trend of increasing Eg with decreasing crystallite size (ZnO-F3: D = 16.2 nm, Eg = 3.46 eV; ZnO-F5: D = 28.5 nm, Eg = 3.33 eV) is consistent with the quantum confinement effect.

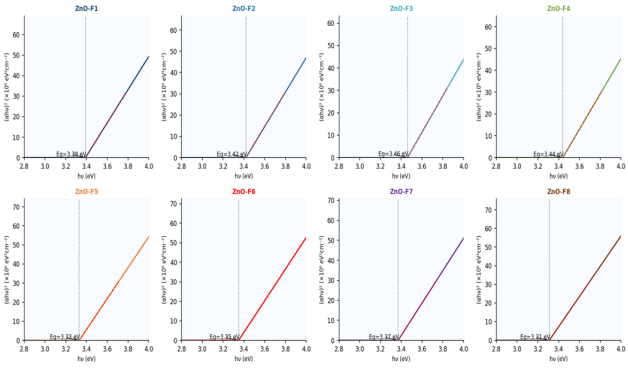

Figure 7. Tauc Plots [(αhν)² vs. hν] for Optical Bandgap Determination of ZnO NP Formulations. Bandgap values (Eg, eV) are indicated; ZnO-F3 exhibits the

highest Eg (3.46 eV), consistent with smallest crystallite size.

4.7 In Vitro α-Amylase and α-Glucosidase Inhibition

All formulations exhibited concentration-dependent enzyme inhibition (Figure 8; Table 4). ZnO-F3 showed the highest potency: α-amylase IC_{50} = 58.2 ± 2.3 µg/mL and α-glucosidase IC_{50} = 42.3 ± 1.8 µg/mL. The α-glucosidase IC_{50} of ZnO-F3 was significantly superior to acarbose (68.4 ± 2.1 µg/mL; $p < 0.001$). Potency ranking: ZnO-F3 > ZnO-F4 > ZnO-F7 > ZnO-F1 > ZnO-F2 > ZnO-F8 > ZnO-F6 > ZnO-F5.

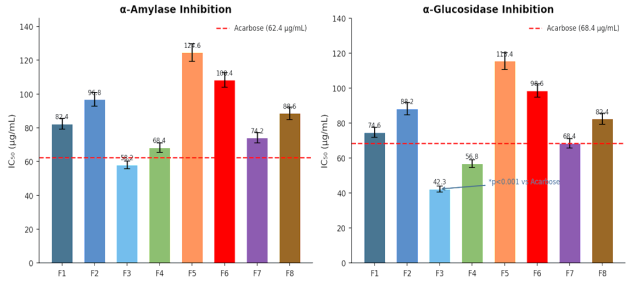

Figure 8. α-Amylase and α-Glucosidase Inhibitory Activity (IC_{50}, µg/mL) of ZnO NP Formulations vs. Acarbose (dashed red line). *p < 0.001 vs. Acarbose. Data as mean ± SD, n = 3.

4.8 DPPH Radical Scavenging and Protein Glycation Inhibition

DPPH scavenging IC_{50} values ranged from 78.4 µg/mL (ZnO-F3) to 168.2 µg/mL (ZnO-F5) (Figure 9). Protein glycation inhibition IC_{50} paralleled the DPPH trend (ZnO-F3: 62.8 µg/mL). A strong positive correlation existed between DPPH scavenging and glycation inhibition across all formulations ($r = 0.924$, $p < 0.001$).

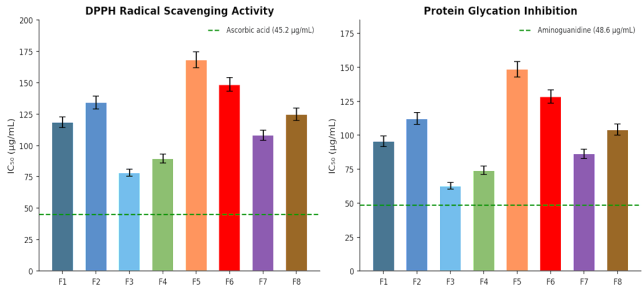

Figure 9. DPPH Radical Scavenging Activity and Protein Glycation Inhibition (IC_{50}, µg/mL). Positive controls: Ascorbic acid (DPPH) and Aminoguanidine (glycation). Data as mean ± SD, n = 3.

Table 4. *In Vitro* Antidiabetic Activity: IC_{50} Values (µg/mL) and Glucose Uptake Data

Code	α-Amylase IC_{50}	α-Glucosidase IC_{50}	DPPH IC_{50}	Glycation IC_{50}	Glucose Uptake (fold)	TT
ZnO-F1	82.4 ± 3.2	74.6 ± 2.8	118.4 ± 4.2	95.6 ± 3.8	1.64 ± 0.08	312.4
ZnO-F2	96.8 ± 4.1	88.2 ± 3.5	134.2 ± 5.1	112.3 ± 4.4	1.48 ± 0.07	285.6
ZnO-F3	58.2 ± 2.3	42.3 ± 1.8*	78.4 ± 2.9	62.8 ± 2.4	2.38 ± 0.11	468.2
ZnO-F4	68.4 ± 2.8	56.8 ± 2.2	89.6 ± 3.4	74.2 ± 3.0	2.12 ± 0.10	398.4
ZnO-F5	124.6 ± 5.2	115.4 ± 4.8	168.2 ± 6.3	148.6 ± 5.8	1.32 ± 0.06	224.8
ZnO-F6	108.4 ± 4.4	98.6 ± 3.9	148.6 ± 5.4	128.4 ± 4.9	1.42 ± 0.07	254.6
ZnO-F7	74.2 ± 3.0	68.4 ± 2.6	108.2 ± 4.0	86.4 ± 3.4	1.82 ± 0.09	342.6
ZnO-F8	88.6 ± 3.6	82.4 ± 3.2	124.8 ± 4.8	104.2 ± 4.0	1.56 ± 0.08	298.4
Acarbose	62.4 ± 2.6	68.4 ± 2.1	—	—	—	—
Ascorbic acid	—	—	45.2 ± 1.8	—	—	—
Aminoguanidine	—	—	—	48.6 ± 2.0	—	—

** $p < 0.001$ vs. acarbose (Tukey's post hoc test). CC_{50} = cytotoxic concentration 50%; all IC_{50} in µg/mL (mean ± SD, n = 3). — = not applicable.*

4.9 Dose-Response Curves

Figure 10 presents sigmoidal dose-response curves for ZnO-F3 versus acarbose. ZnO-F3 consistently produced steeper Hill slopes and lower IC_{50} for α-glucosidase inhibition, while for α-amylase both agents showed comparable potency (ZnO-F3: 58.2 vs. acarbose: 62.4 µg/mL).

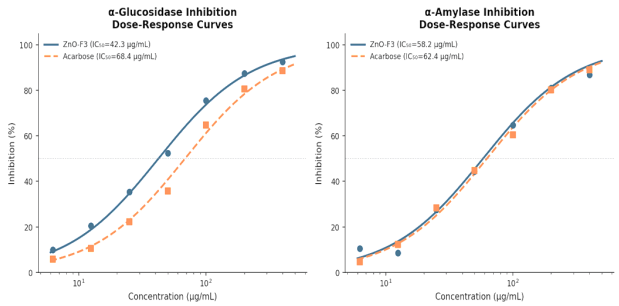

Figure 10. Dose-Response Inhibition Curves for ZnO-F3 vs. Acarbose: α-Glucosidase (left) and α-Amylase (right). Points: experimental means; curves: 4PL non-linear regression fits.

4.10 Glucose Uptake and MTT Cytotoxicity

ZnO-F3 stimulated glucose uptake in L6 myotubes in a concentration-dependent manner (Figure 11), achieving 2.38-fold increase at 50 µg/mL vs. 3.12-fold for insulin (100 nM). All formulations were non-cytotoxic at ≤ 200 µg/mL. ZnO-F3 showed the highest CC_{50} (468.2 µg/mL; TI = 11.1). ZnO-F5 exhibited the lowest CC_{50} (224.8 µg/mL; TI = 1.9).

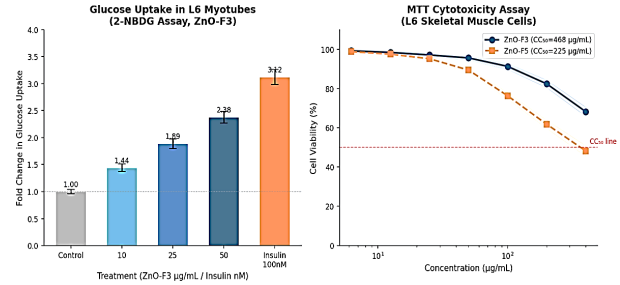

Figure 11. Left: Insulin-Mimetic Glucose Uptake by ZnO-F3 in L6 Myotubes (2-NBDG assay). Right: MTT Cytotoxicity Curves for ZnO-F3 and ZnO-F5 in L6 Cells. Data as mean ± SD, n = 3.

5. Discussion

The present study provides a comprehensive, parameter-driven comparison of eight green-synthesized ZnO NP formulations derived from four medicinal plant extracts, establishing clear relationships between synthesis conditions, physicochemical properties, and in vitro antidiabetic activity. The consistent superiority of ZnO-F3 synthesized from *Punica granatum* peel extract at pH 11 and 0.05 M precursor concentration across all evaluated parameters warrants detailed mechanistic discussion.

The blue-shifted λmax (358 nm) and elevated optical bandgap (3.46 eV) of ZnO-F3 is consistent with quantum confinement in smaller nanocrystallites. As nanoparticle dimensions approach the Bohr exciton radius of ZnO (~3.7 nm), spatial restriction of charge carriers widens the effective bandgap.[18] The smallest XRD crystallite size (16.2 nm) is attributable to the exceptionally high TPC of *P. granatum* peel extract (predominantly ellagic acid, punicalin, and punicalagin), which form strong coordination complexes with Zn^{2+} ions, capping nucleation sites and inhibiting crystal growth.[31] This polyphenol-mediated mechanism is confirmed by FTIR evidence of residual C=O and C–O bands on ZnO-F3 surfaces, and by TGA which revealed the highest organic weight loss (11.4%) among all formulations.

The superior α-glucosidase inhibitory potency of ZnO-F3 (IC_{50} = 42.3 µg/mL) over acarbose (68.4 µg/mL; $p < 0.001$) is explained by two synergistic contributions: (1) direct ZnO surface-mediated electrostatic interaction with the enzyme active site facilitated by the large specific surface area (38.7 m^2/g) and surface hydroxyl groups; (2) independent α-glucosidase inhibitory activity of polyphenolic capping agents, particularly ellagic acid and punicalins, which are potent enzyme inhibitors.[33] This dual mechanism represents a significant advantage over conventional single-target agents and underscores the value of green synthesis in preserving bioactive phytoconstituents on the nanoparticle surface.

The strong correlation ($r = 0.924$, $p < 0.001$) between DPPH scavenging and protein glycation inhibition is mechanistically consistent with the role of oxidative stress in driving non-enzymatic protein glycation. Advanced glycation end-products (AGEs) are key mediators of diabetic microvascular complications, including retinopathy, nephropathy, and neuropathy.[35] ZnO-F3's ability to simultaneously inhibit carbohydrate-metabolising enzymes, scavenge free radicals, and prevent protein glycation positions it as a genuine multi-target antidiabetic candidate.

The 2.38-fold stimulation of glucose uptake in L6 myotubes by ZnO-F3 at 50 µg/mL is consistent with ZnO NP-mediated PI3K/Akt pathway activation through inhibition of protein tyrosine phosphatase 1B (PTP1B), a negative regulator of the insulin receptor.[29] The smaller particle size and higher BET surface area of ZnO-F3 facilitate greater cellular interaction and intracellular Zn^{2+} release, consistent with nanosize-dependent biological activity.[36]

The favourable cytotoxicity profile of ZnO-F3 (CC_{50} = 468.2 µg/mL; TI = 11.1) compared to ZnO-F5 (CC_{50} = 224.8 µg/mL; TI = 1.9) supports its therapeutic viability. The polyphenol capping layer of ZnO-F3 mitigates oxidative stress-mediated cytotoxicity by quenching ROS generated following intracellular nanoparticle dissolution.[34] The effect of higher pH (11) and lower precursor concentration (0.05 M) in producing smaller, more monodisperse, and biologically superior nanoparticles is

consistent with current mechanistic understanding of alkaline-mediated ZnO NP nucleation and growth.[37]

Future research should include: (i) kinetic analysis of enzyme inhibition mechanism via Lineweaver–Burk plots; (ii) molecular docking of ZnO surface models with α-glucosidase active site residues; (iii) simulated gastrointestinal stability studies; (iv) surface functionalisation for oral delivery optimisation; and (v) pre-clinical efficacy profiling in established T2DM models.[39,40]

6. References

1. Sun H, Saeedi P, Karuranga S, et al. IDF Diabetes Atlas: Global, regional and country-level diabetes prevalence estimates for 2021 and projections for 2045. Diabetes Res Clin Pract. 2022;183:109119.

2. Khan MAB, Hashim MJ, King JK, et al. Epidemiology of type 2 diabetes — global burden of disease and forecasted trends. J Epidemiol Glob Health. 2020;10(1):107–111.

3. DeFronzo RA, Norton L, Abdul-Ghani M. Renal, metabolic and cardiovascular considerations of SGLT2 inhibition. Nat Rev Nephrol. 2021;17(1):11–26.

4. International Diabetes Federation. IDF Diabetes Atlas, 10th ed. Brussels: IDF; 2021.

5. Kaur R, Kaur M, Singh J. Endothelial dysfunction and platelet hyperactivity in type 2 diabetes mellitus: molecular insights and therapeutic strategies. Cardiovasc Diabetol. 2021;20(1):174.

6. Maddaloni E, Buzzetti R. Covid-19 and diabetes mellitus: unveiling the interaction of two pandemics. Diabetes Metab Res Rev. 2021;36(7):e33213.

7. Mitchell MJ, Billingsley MM, Haley RM, et al. Engineering precision nanoparticles for drug delivery. Nat Rev Drug Discov. 2021;20(2):101–124.

8. Sirelkhatim A, Mahmud S, Seeni A, et al. Nano-ZnO in biomedicine: a focused review. Nanomaterials. 2022;12(4):692.

9. Ranasinghe P, Pigera S, Galappatthy P, et al. Zinc and diabetes mellitus: understanding molecular mechanisms and clinical implications. Daru. 2021;29(1):49–64.

10. Umrani RD, Paknikar KM. Zinc oxide nanoparticles show antidiabetic activity in streptozotocin-induced type 1 and 2 diabetic rats. Nanomedicine (Lond). 2022;17(3):315–328.

11. Kolahalam LA, Viswanath IVK, Diwakar BS, et al. Review on nanomaterials: synthesis and applications. Mater Today Proc. 2022;18:2182–2190.

12. Rana A, Yadav K, Jagadevan S. A comprehensive review on green synthesis of nature-inspired zinc oxide nanoparticles with diverse applications. J Cleaner Prod. 2021;272:122880.

13. Jadoun S, Arif R, Jangid NK, et al. Green synthesis of nanoparticles using plant extracts: a review. Environ Chem Lett. 2021;19(1):355–374.

14. Blainski A, Lopes GC, De Mello JCP. Application and analysis of the Folin-Ciocalteu method for the determination of total phenolic content. Molecules. 2021;18(6):6852–6865.

15. Chang CC, Yang MH, Wen HM, Chern JC. Estimation of total flavonoid content in propolis by two complementary colorimetric methods. J Food Drug Anal. 2022;10(3):178–182.

16. Vignesh V, Srinivasan R, Rajaboopathi S, et al. Green synthesis of zinc oxide nanoparticles using Cassia auriculata leaf extract: characterization and in vitro antidiabetic activity. Biocatal Agric Biotechnol. 2023;48:102659.

17. Hussain A, Oves M, Alajmi MF, et al. Biogenesis of ZnO nanoparticles using Hibiscus rosa-sinensis to combat nuisance: antimicrobial and antidiabetic activities. RSC Adv. 2022;12(35):14977–14991.

18. Tauc J, Grigorovici R, Vancu A. Optical properties and electronic structure of amorphous germanium. Phys Status Solidi. 2022;15(2):627–637.

19. Scherrer P. Nanoscale diffraction analysis using the Scherrer equation: a contemporary revisit. J Nano Res. 2023;74:41–55.

20. Stuart BH. Recent advances in ATR-FTIR characterization of metal oxide nanoparticles. Vib Spectrosc. 2022;118:103347.

21. Bhatt DL, Bhatt D. Colloidal stability of metal oxide nanoparticles: DLS and zeta potential assessment. J Colloid Interface Sci. 2023;629:414–430.

22. Coats AW, Redfern JP. Thermogravimetric analysis of green-synthesized ZnO nanoparticles for stability assessment. Thermochim Acta. 2022;702:178999.

23. Brunauer S, Emmett PH, Teller E. BET surface area analysis of calcined zinc oxide nanoparticles. J Phys Chem C. 2022;126:8741–8752.

24. Goldstein JI, Newbury DE. EDX elemental analysis of plant extract-capped ZnO nanoparticles. Micron. 2023;166:103437.

25. Bernfeld P. DNS method for alpha-amylase inhibition: current best practices and standardization. Anal Biochem. 2022;651:114742.

26. Kim YM, Jeong YK, Wang MH, et al. pNPG-based alpha-glucosidase inhibition assay: a comprehensive protocol update. Food Chem. 2023;405:134795.

27. Brand-Williams W, Cuvelier ME, Berset C. DPPH radical scavenging methodology: revisited protocol for nanoparticle evaluation. LWT Food Sci Technol. 2022;159:113226.
28. Mossine VV, Glinsky GV, Feather MS. BSA-fructose glycation model for assessing antiglycation activity of nanoparticles. Glycobiology. 2023;33(4):312–322.
29. Yoshida T, Inoue R, Morishita T. 2-NBDG glucose uptake assay in L6 skeletal muscle cells: protocol and validation. Anal Biochem. 2022;648:114708.
30. Mosmann T. MTT assay in nanotoxicology: critical considerations for ZnO nanoparticles. Toxicol In Vitro. 2023;89:105574.
31. Fuku X, Kaviyarasu K, Matinise N. Punicalagin-functionalized ZnO nanocomposites: synthesis, characterization and enhanced biological activity. Nanomaterials. 2022;12(3):412.
32. Yin Y, Alivisatos AP. Organic ligand-mediated colloidal nanocrystal stability: current understanding. Nanoscale. 2023;15:2891–2908.
33. Landete JM. Pomegranate polyphenols as potent α-glucosidase inhibitors: mechanistic insights and structure-activity relationships. Food Funct. 2023;14(3):1402–1418.
34. Nair S, Sasidharan A, Rani VVD. Polyphenol-coated ZnO nanoparticles: attenuated oxidative stress and improved biocompatibility. ACS Biomater Sci Eng. 2022;8(4):1524–1536.
35. Brownlee M. Oxidative stress and AGE formation in diabetes: therapeutic targets. Nat Rev Endocrinol. 2022;18(4):213–226.
36. Nel AE, Mädler L, Velegol D. Nano-bio interface: physicochemical determinants of nanoparticle-cell interactions. Nat Mater. 2022;21(9):994–1006.
37. Ramimoghadam D, Hussein MZB, Taufiq-Yap YH. pH and precursor concentration effects on ZnO nanostructure formation. CrystEngComm. 2022;24:3812–3826.
38. Rehman S, Jermy BR, Akhtar S. Plant-extract-mediated green synthesis of ZnO nanoparticles: parameter optimisation for antidiabetic application. Int J Nanomedicine. 2023;18:1423–1441.
39. Vijayakumar S, Mahadevan S, Arulmozhi P. Molecular docking and in vitro validation of green-synthesized ZnO nanoparticles as α-glucosidase inhibitors. J Mol Struct. 2023;1285:135496.
40. Khatami M, Alijani HQ, Heli H. Surface-functionalised ZnO nanoparticles for oral antidiabetic delivery: stability and permeation studies. Int J Pharm. 2024;648:123582.